Targeting Refractory Mantle Cell Lymphoma for Imaging and Therapy Using C-X-C Chemokine Receptor Type 4 Radioligands

Daniel Kwon[1], Katsuyoshi Takata[2,3], Zhengxing Zhang[1], Lauren Chong[2], Bryan Fraser[1], Jutta Zeisler[1], Tomoko Miyata-Takata[2], Helen Merkens[1], Julie Rousseau[1], Tomohiro Aoki[2], Hsiou-Ting Kuo[1], Ruiyan Tan[1], Chengcheng Zhang[1], Joseph Lau[1], Diego Villa[2], Carlos F. Uribe[1,4], Kuo-Shyan Lin[1,4], Christian Steidl[2,5], and Francois Benard[1,4]

ABSTRACT

Purpose: Mantle cell lymphoma (MCL) is associated with poor survival. The purpose of this study was to assess whether the C-X-C chemokine receptor type 4 (CXCR4) is a useful target for imaging and radioligand therapy of MCL, using a novel pair of radioligands, [68Ga]Ga and [177Lu]Lu-BL02.

Experimental Design: We performed a retrospective analysis of 146 patients with MCL to evaluate CXCR4 expression and its correlation with outcomes. Guided by *in silico* methods, we designed BL02, a new radioligand labelled with 68Ga or 177Lu for PET imaging and therapy, respectively. We performed imaging and biodistribution studies in xenograft models with varying CXCR4 expression. We evaluated [177Lu]Lu-BL02 in MCL models, and evaluated its potential for therapy in Z138 MCL xenografts.

Results: Phosphorylated and nonphosphorylated CXCR4 expression were correlated with poor survival in patients with MCL and characterized by unique underlying molecular signatures. [68Ga]Ga-BL02 uptake correlated with CXCR4 expression, and localized lesions in a metastatic xenograft model. [177Lu]Lu-BL02 showed high uptake in MCL xenografts. Therapy studies with a single dose in the Z138 model showed tumor regression and improved survival compared with a control group. Upon regrowth, the treated mice experienced concurrent metastasis alongside localized xenograft regrowth, and recurrent lesions showed enhanced CXCR4 signaling.

Conclusions: CXCR4 is an independent factor of poor prognosis for MCL and a promising target for imaging and radioligand therapy. [68Ga]Ga-BL02 showed high contrast to visualize CXCR4-expressing xenografts for PET imaging and [177Lu]Lu-BL02 induced rapid tumor regression in a preclinical model of MCL.

Introduction

Mantle cell lymphoma (MCL) is a subtype of B-cell Non-Hodgkin lymphoma that often presents with an aggressive phenotype and is incurable with standard chemotherapies (1, 2). Because of its heterogeneous presentation and poor outcomes, risk stratification strategies such as MCL international prognostic index (MIPI; ref. 3) and biomarkers such as TP53 and SOX11 (4) are used to identify patients with worse prognoses to guide treatment regimens. Currently, no curative strategy exists for aggressive and refractory MCLs (5). Treat-

ments are generally intensive, combining multiple chemotherapeutic agents (e.g., R-CHOP, R-HyperCVAD), followed by autologous stem cell transplant after myeloablation (6, 7). Currently, the use of BTK inhibitors (8), bortezomib (9), epigenetic agents (10), and immunomodulatory agents (11) have shown some promise for the treatment of MCL. Nonetheless, patients still inevitably relapse with refractory disease (5). Furthermore, most treatment regimens have wide-ranging systemic toxicity, excluding many patients who may not be eligible due to age or comorbidities.

The recurrence of MCL is thought to be in part due to minimal residual disease, wherein primary MCL cells are protected from chemotherapy in the stromal niche of the marrow (12, 13). The C-X-C chemokine receptor 4 (CXCR4) has been shown to mediate the homing of MCL cells to the stromal niche, which contains high concentration of SDF-1, CXCR4's endogenous ligand (14). Other roles of CXCR4 include upregulating proliferative signaling pathways such as the Ras/Raf and PI3K/Akt pathways, and potentiating metastases (15, 16). As such, CXCR4 expression in hematologic malignancies is correlated with an aggressive phenotype and propensity for rapid infiltration and dissemination (17).

Radiotheranostics is an emerging method wherein a radiopharmaceutical can bind to a target overexpressed in cancer for imaging or therapy, depending on the radioisotope (18, 19). PET radiotracers can be leveraged not only for diagnostic and monitoring purposes but also to identify patients with sufficient target expression for targeted therapy. PET imaging can also be used for dosimetry calculations to minimize off-target radiotoxicity in healthy organs (20). The success of this approach is exemplified by the development of somatostatin- and prostate-specific membrane antigen-targeting radiopharmaceuticals (21, 22). A CXCR4-targeting radiotheranostic pair, [68Ga]Ga-

[1]Molecular Oncology, British Columbia Cancer, Vancouver, British Columbia, Canada. [2]Centre for Lymphoid Cancer, British Columbia Cancer, Vancouver, British Columbia, Canada. [3]Division of Molecular and Cellular Pathology, Niigata University Graduate School of Medical and Dental Sciences, Asahimachi-dori, Chuo-ku, Niigata, Japan. [4]Department of Radiology, University of British Columbia, Vancouver, British Columbia, Canada. [5]Department of Pathology and Laboratory Medicine, University of British Columbia, Vancouver, British Columbia, Canada.

Translational Relevance

Mantle cell lymphoma (MCL) is an uncommon subtype of B-cell malignancies with variable biological behavior. Treatment-refractory disease and relapse are common, resulting in poor 5-year survival rates. Methods to identify patients with poor prognosis and accurately localize disease sites would be useful for patient stratification and staging. New lines of effective treatment modalities are also needed for patients with refractory or relapsed disease, or as an alternative to high-dose chemo-therapy with autologous stem cell transplantation. We demonstrated an association between CXCR4 expression and poor outcomes in patients with MCL and showed the importance of the functional status of CXCR4 and its association with gene expression profiles. We characterized a novel peptide-based radiotracer targeting CXCR4, BL02, for PET imaging and radio-oligand therapy of MCL. We demonstrated that [^{68}Ga]Ga-BL02 showed high contrast imaging in multiple MCL xenografts, and [^{177}Lu]Lu-BL02 was effective in inducing tumor regression in a MCL xenograft model.

Pentixafor and [^{90}Y]Y/[^{177}Lu]Lu-Pentixather, have shown promise in small clinical studies and is currently being evaluated in clinical trials (23, 24).

The potential benefit of identifying and monitoring CXCR4-expressing lymphomas coupled with their high-radiation sensitivity led us to develop an improved peptide-based CXCR4-targeting radiotheranostic. The purpose of this study was to evaluate the expression of CXCR4 in a retrospective cohort of patients with MCL, and its association with prognosis. We also explored the association between CXCR4 expression, and gene expression profiles in a subset of patients with MCL with RNA sequencing (RNA-seq) data. Improving on prior work with a CXCR4-targeted radio-theranostic derived from the LY2510924 peptide backbone (25), we designed, synthesized, and evaluated [^{68}Ga]Ga-/[^{177}Lu]Lu-BL02 as a new radiotracer to visualize and treat MCL CXCR4-expressing MCL xenografts.

Materials and Methods

Details on the cell line RNA-seq, flow cytometry, chemical synthesis, *in silico* docking, cell lines, radiolabeling methods, *in vitro* characterization of radiotracers, xenograft growth conditions, dosimetry, and statistical analyses are provided in the Supplementary Information.

IHC antibodies

IHC analyses of tissues were performed using the following antibodies: nonphosphorylated CXCR4 (npCXCR4; UMB-2; Abcam/Epitomics), phosphorylated CXCR4 (pCXCR4; pSer^{339}, rabbit polyclonal; Sigma-Aldrich), CD20 (clone L26; DAKO), and Ki-67 (clone MIB-1; DAKO).

IHC analysis of MCL biopsy samples

A retrospective study of a single-center patient cohort at BC Cancer consisted of biopsies of 146 unique patients with MCL with a follow-up period of a median of 5.4 years (range: 0.2–14.7 years) with previously disclosed inclusion and exclusion criteria (26). This study was approved by the BC Cancer REB in accordance with the Declaration

of Helsinki and all participants were recruited with informed consent (H14–02304 and H18–00469). IHC analysis for npCXCR4 and pCXCR4 was performed on formalin-fixed paraffin-embedded (FFPE) tissue of tissue microarrays (TMA) of 146 MCL cases (26). Staining was performed on a Benchmark XT platform (Roche). pCXCR4 expression was quantified by assigning a histoscore out of 200, which was calculated by multiplying the value for staining intensity (0–2) with the percentage of positive tumor cells (0–100). A histoscore of 80 (median value) was determined to be the cut-off score between high and low expression of pCXCR4. Biopsies were considered positive for npCXCR4 expression if >5% of tumor cells showed positive membrane staining followed by the previously published criteria (27). CXCR4 and pCXCR4 protein expression were independently evaluated by two experienced hematopathologists (K. Takata and T. Miyata-Takata), both of whom were blinded when scoring.

RNA-seq analysis of patient samples

For 72 of the MCL biopsy samples, previously published RNA-seq libraries were available (26). Details on the sample processing are described in the Supplementary Data section. Differential expression was performed with the DESeq2 R package (28) using various discriminating features to separate samples based on their IHC profile (i.e., CXCR4 and pCXCR4 status). Using the Database for Annotation, Visualization and Integrated Discovery (DAVID v6.8; refs. 29, 30) enrichment analysis, each gene was assigned a differential expression (DE) score calculated as:

$$score = -\log 10(pval) \times sign(\log 2FC)$$

where pval is the DE *P* value and log2FC is the log$_2$-adjusted fold change from the DE comparison. Two gene lists were generated representing the top 250 upregulated (positive score) and downregulated (negative score) genes. Each of these was submitted as a list of gene names to DAVID v6.8 to discover enriched pathways using the GO (31, 32), KEGG (33), and Biocarta (34) annotation databases (human annotations only and human background). Enrichment was also performed using gene set pre-enrichment analysis (GSEA Pre-Ranked v4.0.2 and v4.1.0; refs. 35, 36), ranking the genes by log2-adjusted fold-change and investigating pathways in the GO and Hallmarks databases.

Animal models

Animal experiments were performed in accordance with guidelines established by the Canadian Council on Animal Care, under a research protocol approved by the Animal Ethics Committee of the University of British Columbia. Cell lines used for *in vivo* studies were authenticated, and tested for potential rodent pathogens and mycoplasma contamination using the IMPACT test (IDEXX BioAnalytics). For all studies, male NOD.Cg-Rag1^{tm1Mom}Il2rg^{tm1Wjl}/SzJ (NRG) mice were used, and cells injected subcutaneously in a 100 μL solution of 1:1 ratio of PBS/Matrigel. Xenograft growth conditions can be found in the Supplementary Data.

IHC for npCXCR4 of subcutaneous xenograft models was performed as outlined for clinical samples. For the Jeko1 metastatic model, IHC for CD20 was performed on FFPET of the femur, liver, lungs, and spleen. IHC analysis of npCXCR4 and pCXCR4 was also determined on FFPET of the femur. For the radioligand therapy study, IHC for Ki-67, CD20, npCXCR4, and pCXCR4 was determined on the FFPET of the tumor of the control group and the tumor, liver, lungs, and spleen of the treatment group. CXCR4 staining intensity was calculated by thresholding three independent high power IHC images

to black and white and measuring the mean grey value using Image J software (ver. 1.48).

PET/CT and SPECT/CT imaging

PET and CT scans were performed on a Siemens Inveon micro-PET/CT. SPECT and CT images were obtained using a MILabs U-SPECT-II/CT scanner. Tumor-bearing mice were briefly sedated with isoflurane (2%–2.5% isoflurane in 2 L/min O_2) for intravenous injection of 4 to 7 MBq of [^{68}Ga]Ga-BL02, or [^{68}Ga]Ga-Pentixafor for PET imaging, or 13.1 to 15.2 MBq of [^{177}Lu]Lu-BL02 for SPECT imaging. Mice received intraperitoneal injection of 7.5 μg (0.25–0.3 mg/kg) of LY2510924 (MedChemExpress), 15 minutes prior to radiotracer administration as blocking controls. The animals were allowed to roam freely during the uptake period (50 or 110 minutes for PET imaging; 1, 4, 24, or 72 hours for SPECT imaging), after which they were sedated and scanned. The parameters of the CT and PET, and CT and SPECT data acquisitions can be found in the Supplementary Materials and Methods.

Biodistribution

Under brief isoflurane sedation (2%–2.5% isoflurane in 2 L/min O_2) for the injection only, the mice were injected intravenously with 0.8 to 3.0 MBq of [^{68}Ga]Ga-BL02, [^{177}Lu]Lu-BL02, or [^{68}Ga]Ga-Pentixafor, allowed to roam freely afterwards in their cage, and euthanized at the selected timepoints. Additional groups of mice received 7.5 μg (0.25–0.3 mg/kg) LY2510924 as a blocking control intraperitoneally 15 minutes before radiotracer injection and euthanized 1 hour p.i.

Radioligand therapy studies

When the Z138 xenografts had grown to a volume of 500 ± 180 mm^3, the mice were randomized into two groups ($n = 8$ each). Z138 xenograft mice were briefly sedated (2%–2.5% isoflurane in 2

L/min O_2) and injected with either [^{177}Lu]Lu-BL02 or PBS (100 μL). Both treatment groups were longitudinally monitored for tumor volume, body weight, and behavior every other day until 60 days or until mice reached the volume endpoint (>1,500 mm^3), loss of body weight (>15%), or unwell behavioral signs (e.g., lethargy, loss of appetite). Tumors were measured using a Biopticon Imager 2. After euthanasia, the tumor was collected for the control group and the tumor, bone (femur and tibia), lungs, liver, kidneys, and spleen were collected for the treatment group.

Data availability

Cell line RNA-seq data were deposited in GEO (accession no. GSE190587).

Results

CXCR4 is widely expressed in hematologic malignancies, including MCL

The Cancer Cell Line Encyclopedia (CCLE) showed relatively high levels of CXCR4 mRNA in hematologic malignancies but had no MCL cell lines within its collection (37). To better assess the suitability of targeting CXCR4 in MCL, we screened 11 MCL cell lines for CXCR4 mRNA expression (Cancer Research Centre, CRC; **Fig. 1A**). For comparison, we profiled other lymphoma subtypes, including Burkitt ($n = 3$), activated B cell–like (ABC) diffuse large B-cell lymphoma (DLBCL; $n = 6$), and germinal center B cell–like (GBC) DLBCL ($n = 14$; Supplementary Figs. S1–S5). On average, all lymphoma cell lines had high mRNA expression of CXCR4, although MCL cell lines had a higher expression of CXCR4 compared with GBC DLBCL ($P < 0.05$). Hematologic malignancy cell lines in both colorectal cancer and CCLE collections showed a significant increase in CXCR4 mRNA expression compared with a randomly selected sample
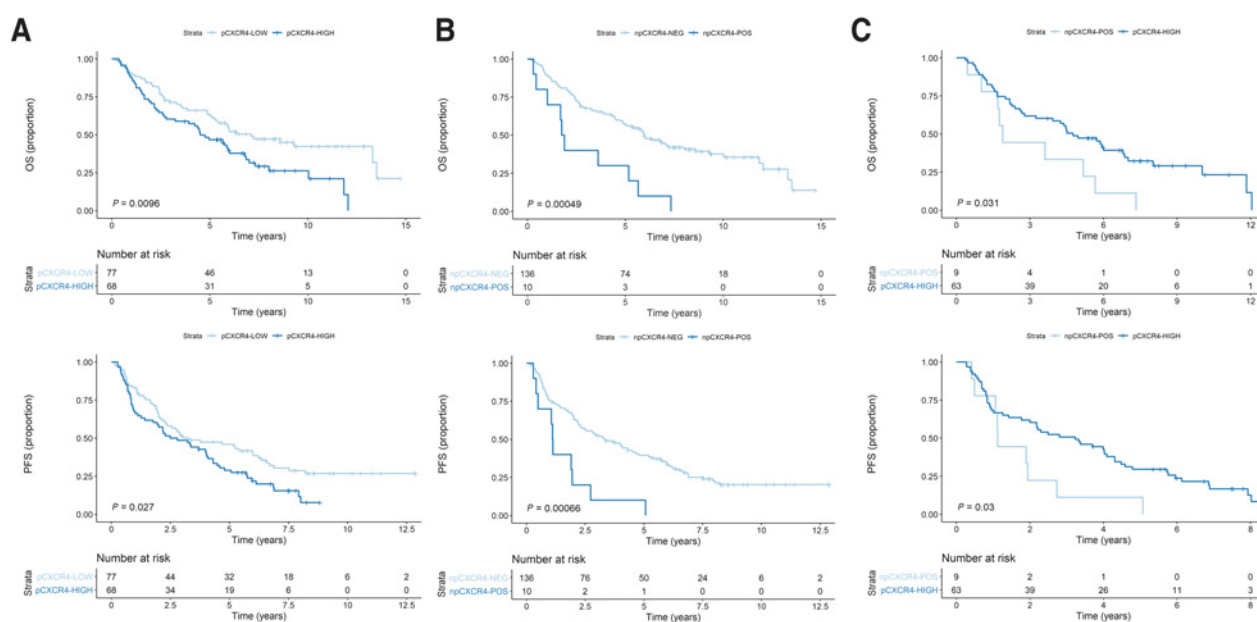

Figure 1.
A, Kaplan–Meier curves assessing OS and PFS of pCXCR4-high ($n = 68$) versus npCXCR4-low ($n = 77$) MCL patients. **B,** Kaplan–Meier curves assessing OS and PFS of npCXCR4-POS ($n = 10$) versus npCXCR4-NEG ($n = 136$) MCL patients. **C,** Kaplan–Meier curves assessing OS and PFS of npCXCR4-POS ($n = 9$) versus pCXCR4-high ($n = 63$) MCL patients.

of other cell lines in the CCLE (Supplementary Fig. S6). The CXCR4 expression levels of the DLBCL and Burkitt lymphoma cell lines in the CCLE were in good agreement with our cell line RNA-seq data when adjusted for batch effects (Supplementary Fig. S4).

CXCR4 is an independent poor prognostic factor in a MCL patient cohort

To study the clinical significance of CXCR4 expression in MCL, we assembled a cohort of 146 patients with MCL uniformly treated with R-CHOP and assessed their CXCR4 expression. Only 10 patients showed positive expression of npCXCR4. However, the UMB-2 antibody is only specific for an unphosphorylated epitope within the receptor's C-terminus tail (38) and not for phosphorylated epitopes upon receptor activation. To enhance the sensitivity for CXCR4 expression and to differentiate MCLs based on active versus inactive CXCR4 signaling, we concurrently used an antibody that is specific for a C-terminal sequence containing a phosphorylated Ser339, a residue that undergoes phosphorylation upon activation of the receptor (39). Reflective of the highly active CXCR4/SDF-1 signaling within the tumor microenvironment, all but 3 patients stained positive for pCXCR4. pCXCR4-high status was determined using the median histoscore (% of positive cells multiplied by an intensity factor) which was 80 of 200.

Using the median histoscore as a cutoff, pCXCR4-high patients showed an inferior 5-year OS (47% vs. 63%, $P = 0.0096$) and PFS (29% vs. 46%, $P = 0.027$) rates as compared with pCXCR4-low patients (**Fig. 1A**). pCXCR4-high status was associated with blastoid morphology ($P = 0.02$), higher ki-67 median index ($P = 0.02$), and recurrent disease ($P = 0.03$; **Table 1**). Using pCXCR4 histoscore as a continuous variable showed correlation with OS ($P = 0.0008$) and PFS ($P = 0.0044$). With respect to npCXCR4-POS patients, 10 of the 146 (6.8%) tumors had positive membrane staining, with a lower 5-year OS (30% vs. 54%, $P = 0.00049$) and PFS (10% vs. 36.8%, $P = 0.00066$) as compared with npCXCR4-NEG patients (**Fig. 1B**). npCXCR4-POS status also conferred a worse 5-year OS (33% vs. 47%, $P = 0.031$) and PFS (11% vs. 30%, $P = 0.03$) as compared with pCXCR4-high status (**Fig. 1C**). Positive staining was associated with a worse ECOG performance status ($P = 0.02$) and MIPI score

Table 1. Summary of clinical characteristics between npCXCR4-POS and -NEG patients and between pCXCR4-high and -low patients.

Parameter	npCXCR4-POS ($n = 10$)	npCXCR4-NEG ($n = 136$)	P value	pCXCR4-high ($n = 68$)	pCXCR4-low ($n = 77$)	P value
BM involvement			0.15			0.62
Present	9	93		46	55	
Absent	1	43		22	22	
Stage (Ann Arbor)			0.6			0.98
I–II	0	15		7	8	
III–IV	10	119		60	68	
na	0	2		1	1	
Age			0.2			0.29
≤60	2	58		25	35	
>60	8	78		43	42	
Sex			0.12			0.67
Female	0	36		18	18	
Male	10	100		50	59	
ECOG PS			0.02			0.98
0–1	3	102		48	57	
2–4	5	28		15	17	
na	2	6		5	3	
LDH			0.28			0.77
Normal	4	82		38	48	
Abnormal	5	43		22	25	
na	1	11		8	4	
MIPI			0.01			0.72
Low	2	87		40	49	
Intermediate	3	26		14	15	
High	5	22		14	12	
na	0	1		0	1	
Ki-67 index median value	30	37.5	0.3[a]	40	25	0.02[a]
Blastoid morphology			0.78			0.02
Present	3	15		13	5	
Absent	7	121		55	72	
Transplantation			0.57			0.07
Yes	3	53		21	35	
No	7	89		47	42	
Recurrence			0.12			0.03
Present	10	101		57	53	
Absent	0	35		11	24	

Abbreviations: BM, bone marrow; MIPI, mantle cell lymphoma international prognostic index; PS, performance status.
[a]Unpaired *t* test.

($P = 0.01$; **Table 1**). All 10 npCXCR4-POS patients presented with recurrent disease but was only significant at a P value of 0.12 (**Table 1**). Multivariate cox regression analysis showed npCXCR4-positive status remained an independent prognostic biomarker for both OS and PFS [$P = 0.022$, HR = 2.9 (95% CI, 1.2–7.2), $P = 0.025$, HR = 2.9 (95% CI, 1.1–7.3); **Table 1**]. However, pCXCR4-high did not reach significance as an independent prognostic biomarker for OS ($P = 0.37$) and PFS ($P = 0.28$). Using pairwise multivariate analysis with the MIPI score (low/intermediate vs. high), positive scoring for both pCXCR4 and npCXCR4 was an independent prognostic biomarker for both OS and PFS, respectively [pCXCR4: OS HR = 1.8 (95% CI, 1.2–2.9) $P = 0.005$, PFS HR = 1.7 (95% CI, 1.1–2.5), $P = 0.008$; npCXCR4: OS HR = 2.1 (95% CI, 1.1–4.3), $P = 0.036$, PFS HR = 2.2 (95% CI, 1.1–4.4), $P = 0.033$]. pCXCR4 showed no association with the site of biopsy ($P = 0.35$). npCXCR4 was not significantly correlated to extranodal biopsy sites ($P = 0.12$). No association between npCXCR4 and pCXCR4 was found ($r = 0.34$, $P = 0.34$).

As pCXCR4-high did not reach significance as an independent prognostic marker, we assessed for the optimal cut-off pCXCR4 histoscore, which was determined to be at 30 (pCXCR4-high$_{30}$) for both OS and PFS (Supplementary Figs. S7 and S8). Kaplan–Meier curves showed a statistically significant difference between the groups at $P < 0.0001$. pCXCR4-high$_{30}$ was shown to be independently prognostic for both OS (HR, 2.9; 95% CI, 1.1–7.2; $P = 0.019$) and PFS (HR, 2.4; 95% CI, 1.2–5.2; $P = 0.019$) in the same multivariate Cox regression analysis. For the pairwise multivariate analysis with MIPI scoring, pCXCR4-high$_{30}$ was also independently prognostic for OS (HR, 4.9; 95% CI, 2.3–10.1; $P < 0.001$) and PFS (HR, 3.6; 95% CI, 2.0–6.4; $P < 0.001$). Finally, to assess whether a range of pCXCR4 histoscore values show a significant difference in survival, we generated survival curves for histoscore cut-offs of 20, 40, 50, 60, and 100, all of which show a statistically significant difference in OS and PFS (Supplementary Fig. S9).

Molecular correlates of pCXCR4+ and npCXCR4+ MCLs

To understand the underlying molecular alterations in the setting of pCXCR4 and npCXCR4 in MCL, we performed differential expression analyses *via* DAVID and GSEA using a subset of 72 patient samples which had accompanying transcriptomics data. In pCXCR4-high cancers, DAVID analysis showed that pathways implicated in cell cycle and division were significantly upregulated, including mitotic nuclear division (fold enrichment = 5.17; FDR = 0.011), mitotic sister chromatid segregation (fold enrichment = 23.32; FDR = 0.011), and cell division (fold enrichment = 3.998; FDR = 0.034). The DNA repair pathway was also upregulated (fold enrichment = 5.46; FDR = 0.011). Downregulated pathways were primarily immune-related responses, including immune response (fold enrichment = 3.60; FDR = 0.017), regulation of immune response (fold enrichment = 7.91; FDR = 0.155E−5), and antigen binding (fold enrichment = 12.9; FDR = 5.17E−7). Similarly, GSEA analysis showed that gene sets related to cell cycle and sensory perception to chemical stimulus were upregulated, whereas downregulated gene sets included T-cell receptor complex and several pertaining to immune-related responses (Supplementary Fig. S10; Supplementary Tables S1–S4).

npCXCR4-POS MCLs also showed downregulation of several immune-related pathways. DAVID analysis showed downregulation of gene sets such as antigen binding (fold enrichment = 14.1; FDR = 1.54E−7), complement binding (fold enrichment = 15.5; FDR = 4.2E−7), and regulation of immune response (fold enrichment = 9.5; FDR = 9.0E−7), whereas GSEA analysis also showed downregulations

in gene sets pertaining to primary and secondary immune reactions and humoral response (Supplementary Fig. S11; Supplementary Tables S5–S8). However, a distinguishing finding was that no T-cell–related immune gene sets were found to be downregulated in npCXCR4-POS MCLs, potentially differentiating their immunological alterations. Gene sets related to downstream CXCR4 signaling were similarly absent.

In silico docking reveals BL02 as a potential candidate

LY2510924 is a highly potent cyclic antagonist of CXCR4 with high specificity over other G-protein–coupled receptors (40). We previously reported a new CXCR4 radiotheranostic pair, [^{68}Ga]Ga/[^{177}Lu]Lu-BL01, which showed high uptake in the CXCR4-expressing Daudi model, with some nontarget accumulation in the lungs, spleen, and liver (25). A tested strategy to enhance excretion and lower nonspecific tissue accumulation of peptide-based radiopharmaceuticals is to conjugate linkers with hydrophilic properties. As other peptide-based CXCR4-targeting radiotracers have shown that linker conjugation can significantly affect binding (41), we used *in silico* docking to identify linkers that would not interfere with the pharmacophore binding. With the LY2510924 ligand as an anchor to an x-ray crystal structure of CXCR4 (42), we found that a triglutamate linker, which is highly hydrophilic, was unlikely to interfere with binding (**Fig. 1A** and **B**). Induced-fit docking suggested the triglutamate linker accesses electrostatic contacts along the CRS2/CRS1.5 interaction axis defined in the SDF1a/CXCR4 complex (43), while optimally placing the bulky, hydrophilic DOTA chelate at the mouth of the receptor. The metal–chelator complex was shown to fit within the electronegative CRS0.5 site enclosed by Glu^2, Glu^{31}, Glu^{179}, Asp^{181}, and Asp^{182}.

Given these results, BL02 was synthesized using solid-phase peptide synthesis (Supplementary Fig. S11). *In vitro* competitive binding assays to calculate the IC$_{50}$ showed that both Ga-BL02 (IC$_{50}$ = 27.9 ± 12.5) and Lu-BL02 (IC$_{50}$ = 22.7 ± 8.4) retained comparable affinity to CXCR4 compared with LY2510924 (IC$_{50}$ = 24.8 ± 2.5). Both Ga-BL02 and Lu-BL02 showed low internalization rates but Lu-BL02 strongly bound to Z138 cells over 3 days (Supplementary Fig. S12; Supplementary Table S10).

Radiosynthesis and preclinical evaluation of [^{68}Ga]Ga-BL02

[^{68}Ga]Ga-BL02 ($n = 12$) was labeled with high molar activity (258 ± 90 Gbq/µmol), radiochemical yield (64.0 ± 9.9%), and purity (>99%), and was shown to be stable *in vivo* based on the assessment of the harvested plasma and urine of injected NRG male mice 5 and 30 minutes p.i., respectively (Supplementary Fig. S13). [^{68}Ga]Ga-BL02 possessed a LogD$_{7.4}$ value of −4.20 ± 0.44. PET images and biodistribution studies of [^{68}Ga]Ga-BL02 in Daudi-bearing xenograft mice showed high tumor uptake at 1 and 2 hours p.i. (8.56 ± 2.25 and 7.78 ± 1.44%ID/g at 1 and 2 hours p.i., respectively) with specificity corroborated by blocking (**Fig. 2C** and **D**). There was comparatively low uptake in nontarget organs, except in the kidneys (3.81 ± 0.81 and 3.40 ± 0.51%ID/g at 1 and 2 hours p.i., respectively), indicating that [^{68}Ga]Ga-BL02 is primarily renally excreted. The continual clearance of radioactivity between 1 and 2 hours p.i. translated into an increase in already-high tumor-to-organ contrast ratios, with tumor-to-blood and tumor-to-muscle ratios of 31.7 ± 12.6 and 79.7 ± 26.7 at 1 hour and 115 ± 44.6 and 216 ± 57.5 at 2 hours p.i., respectively.

For comparison, Pentixafor was radiolabeled with [^{68}Ga]GaCl$_3$ and assessed in the same xenograft model (**Fig. 2C** and **D**). [^{68}Ga]Ga-Pentixafor showed lower tumor uptake values ($P = 0.0009$ at 1 hour p.i. and $P = 0.0007$ at 2 hours p.i.; **Fig. 2E** and **F**). [^{68}Ga]Ga-Pentixafor's
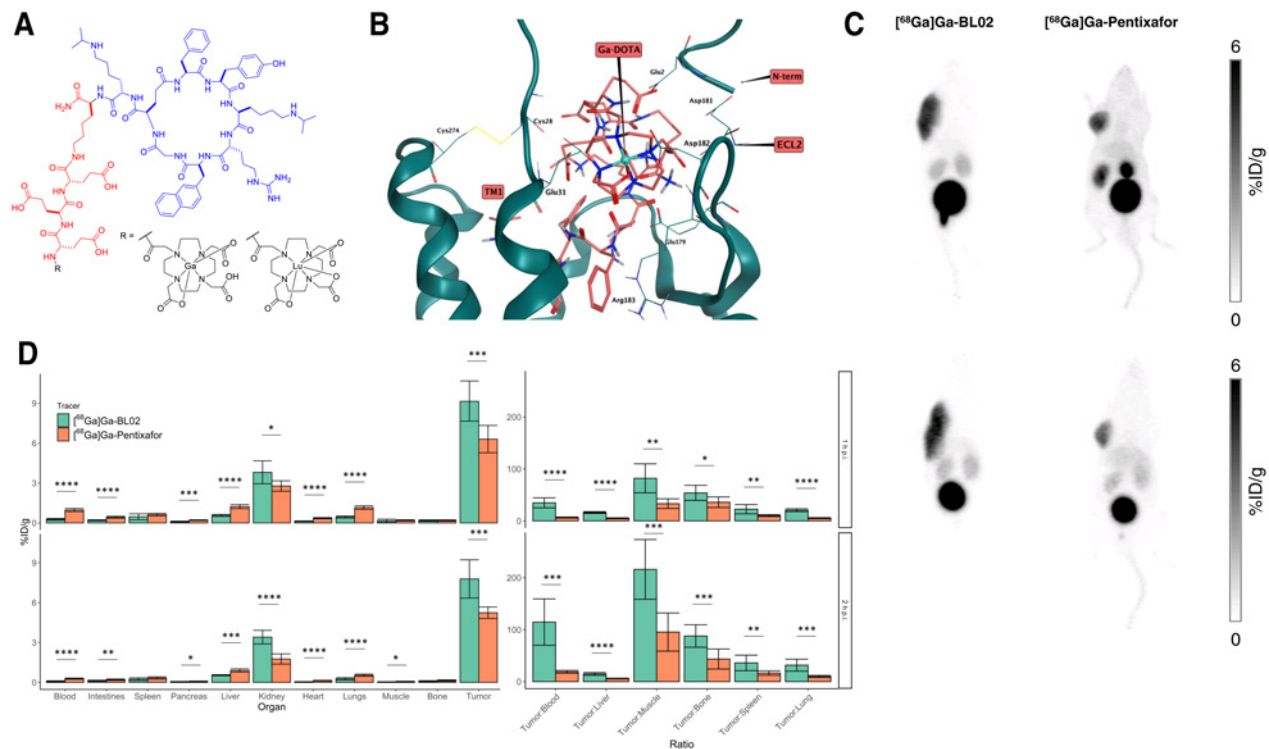
Figure 2.
A, Structure of Ga- and Lu-BL02 with the LY2510924 pharmacophore in blue, the lysine-triglutamate linker in red, and the metal–chelator complex in black. **B,** *In silico* docking of Ga-BL02 to a previously disclosed x-ray crystal structure of CXCR4 complexed to a cyclic peptide. **C,** Maximum intensity projections of PET images of [^{68}Ga]Ga-BL02 and [^{68}Ga]Ga-Pentixafor injected in Daudi xenograft-bearing mice at 1 hour (top) and 2 hours (bottom) p.i. Scale of the PET images is 0%ID/g to 6%ID/g. **D,** *Ex vivo* biodistribution data of [^{68}Ga]Ga-BL02 and [^{68}Ga]Ga-Pentixafor in Daudi xenograft-bearing mice at 1 and 2 hours p.i. (*, $P < 0.05$; **, $P < 0.01$; ***, $P < 0.001$; ****, $P < 0.0001$).

higher background activity translated to lower contrast ratios, with tumor-to-blood and tumor-to-muscle of 6.53 ± 0.97 ($P < 0.0001$) and 33.3 ± 9.3 ($P = 0.0013$) at 1 hour p.i., respectively, and 18.9 ± 2.7 ($P = 0.0002$) and 95.4 ± 36.7 ($P = 0.0002$) at 2 hours p.i.

Quantifying CXCR4 expression by [^{68}Ga]Ga-BL02 PET imaging

On the basis of the RNA-seq data, we assessed several cell lines including high (SP-53, Z138, Jeko1, SP-49) and low (GRANTA519 and REC1) CXCR4 expressing MCL cell lines for *in vitro* surface-level CXCR4 expression using FACS with Daudi (positive) and PC3 (negative/low) as controls. The FACS results correlated well with the RNA-seq data (Supplementary Fig. S14). For *in vivo* PET imaging and biodistribution studies, Z138, Jeko1, and GRANTA519 were selected to further assess the sensitivity of [^{68}Ga]Ga-BL02 with PC3 xenografts as a negative/low control (**Fig. 3A** and **B**; Supplementary Figs. S15–S19). Biodistribution studies of Z138, Jeko1, and GRANTA519 MCL xenograft mice at 1 hour p.i. showed tumor uptake values of 12.9 ± 1.3, 11.5 ± 1.1, and 5.5 ± 1.0%ID/g. Low uptake (1.94 ± 0.42%ID/g) was observed in PC3 xenografts but specificity was confirmed on the basis of blocking (0.75 ± 0.26%ID/g, $P = 0.00041$). As Z138 had only a slightly higher CXCR4 expression than Jeko1 based on flow cytometry, the difference in uptake of [^{68}Ga]Ga-BL02 was not significant ($P = 0.24$), whereas all the other differences based on rank were statistically significant.

However, the *in vivo* PET imaging data were not completely consistent with the *in vitro* FACS data. To validate these results, xenografts were harvested and evaluated *ex vivo* by flow cytometry and IHC. IHC staining for npCXCR4 showed intensities of 27.8 ± 2.0, 22.5 ± 3.0, 13.54 ± 2.11, 11.3 ± 0.9, and 1.16 ± 0.24 for the Z138, Jeko1, Daudi, GRANTA519, and PC3 xenografts, respectively, correlating with the order of uptake of [^{68}Ga]Ga-BL02 (**Fig. 3C**). The *ex vivo* flow cytometry data further corroborated these results (**Fig. 3D**).

[^{68}Ga]Ga-BL02 identifies metastatic lesions in Jeko1 xenograft model

Inspection of the PET images and biodistribution data of Jeko1 xenograft mice showed relatively high uptake in the bone marrow. Given that the Jeko1 cell line was derived from the peripheral blood of a patient with MCL undergoing leukemic conversion (44), we hypothesized that this uptake was due to metastasis. [^{68}Ga]Ga-BL02 PET imaging of a cohort of Jeko1 xenograft mice ($n = 4$) showed extensive disease infiltration throughout the body, including the liver and lungs, compared with PC3 xenograft mice (**Fig. 3A–C**; Supplementary Fig. S20). Positive infiltration of Jeko1 cells in the bone marrow, spleen, liver, and lungs were confirmed using IHC staining for CD20 (**Fig. 3D–G**). Biodistribution studies of the imaged mice showed a statistically significant increase in activity uptake in these organs compared with the PC3 biodistribution data (**Fig. 3H**). Finally, IHC analysis of the bone marrow showed a high ratio of pCXCR4:npCXCR4 (**Fig. 3I**).

[^{177}Lu]Lu-BL02 shows high uptake in CXCR4-expressing tumors with little uptake in healthy tissues

[^{177}Lu]Lu-BL02 was labeled with [^{177}Lu]LuCl$_3$ at a molar activity of 247.65 ± 28.95 Gbq/µmol and a radiochemical yield and purity of
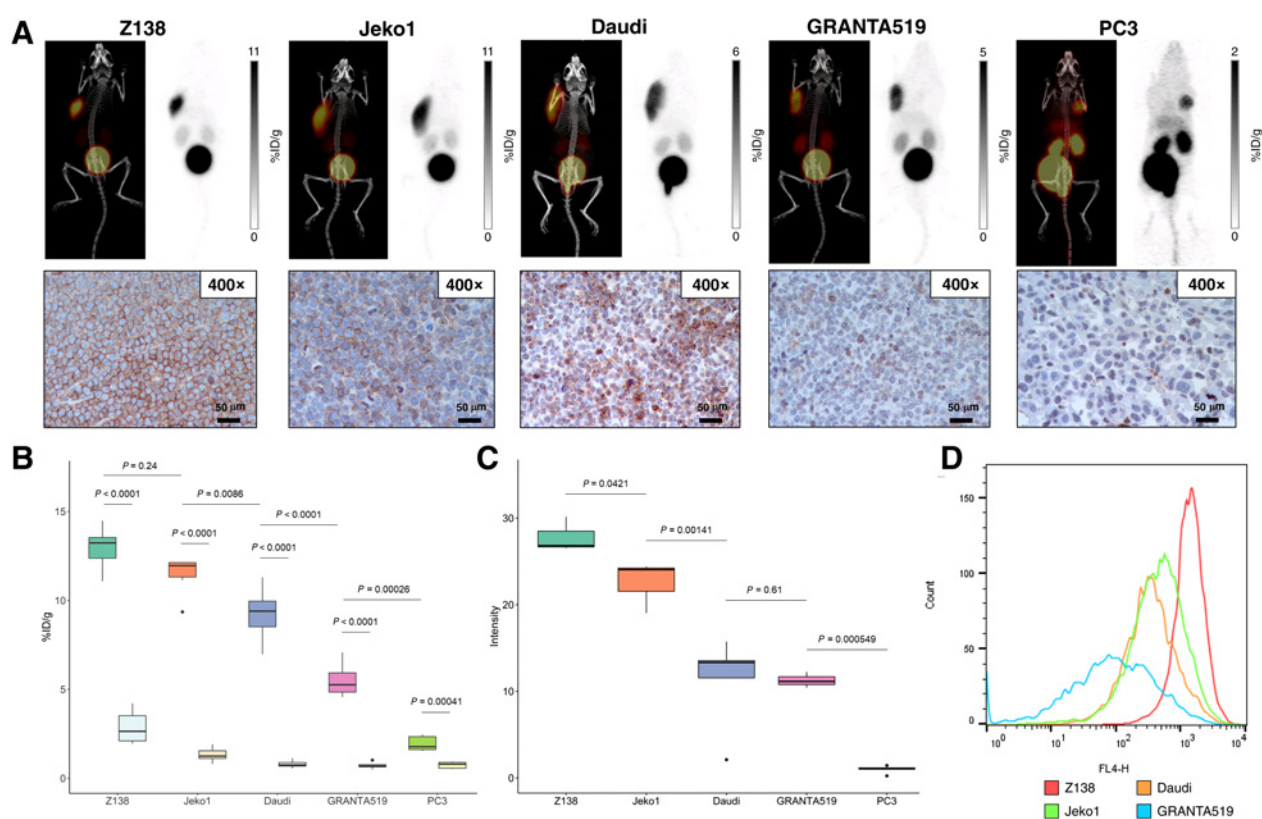
Figure 3.
A, Maximum intensity projections of PET images of [^{68}Ga]Ga-BL02 in Z138, Jeko1, Daudi, GRANTA519, and PC3 xenograft-bearing mice at 1 hour p.i. with an accompanying anti-CXCR4 IHC staining of the xenograft tissue at 400× magnification. Scales of the PET images are indicated in each image. **B,** Tumor uptake values (%ID/g) in Z138, Jeko1, Daudi, GRANTA519, and PC3 xenograft-bearing mice at 1 hour p.i. via an *ex vivo* biodistribution study (left). The accompanying tumor uptake value (%ID/g) in Z138, Jeko1, Daudi, GRANTA519, and PC3 xenograft-bearing mice at 1 hour p.i. with a blocking agent (right). The LY2510924 blocking agent was injected intraperitoneally 15 minutes prior to [^{68}Ga]Ga-BL02 injection. **C,** The *ex vivo* staining intensities of the anti-CXCR4 IHC analysis of Z138, Jeko1, Daudi, GRANTA519, and PC3 xenograft. **D,** Flow cytometry analysis assessing CXCR4 membrane expression of Z138, Jeko1, Daudi, and GRANTA519 xenograft cells.

67.5 ± 4.4% and >99%, respectively. The longitudinal biodistribution of [^{177}Lu]Lu-BL02 was studied in Z138 and GRANTA519 xenograft mice via SPECT imaging and biodistribution studies, which showed tumor uptake values reflecting the expression of CXCR4 (Supplementary Figs. S21 and S22). [^{177}Lu]Lu-BL02 showed tumor uptake values of 17.17 ± 3.04, 15.57 ± 2.59, 8.79 ± 1.22, and 3.57 ± 0.65%ID/g at 1, 4, 24, and 72 hours p.i., respectively, in Z138 xenografts. In GRANTA519 xenografts, [^{177}Lu]Lu-BL02 showed tumor uptake values of 6.83 ± 1.26, 3.22 ± 0.49, 1.09 ± 0.13, and 0.35 ± 0.03%ID/g at 1, 4, 24, and 72 hours p.i., respectively. Specificity was confirmed with blocking controls. Compared with [^{68}Ga]Ga-BL02, [^{177}Lu]Lu-BL02 showed higher uptake in Z138 ($P = 0.01$; Supplementary Fig. S23) and in GRANTA519 xenografts ($P = 0.0704$). [^{177}Lu]Lu-BL02 cleared quickly from the circulation, with a >90% decrease in blood pool radioactivity between 1 and 4 hours p.i., and low uptake in nontarget organs, except the kidneys, at all timepoints. This translated into very high tumor-to-organ ratios in the Z138 xenograft mice, with an increase from 39.0 ± 3.0 to 630 ± 130 tumor-to-blood ratio and 167 ± 14 to 503 ± 127 tumor-to-muscle ratio from 1 to 4 hours p.i. The high tumor-to-organ ratios were maintained at both 24 hours (tumor-to-blood and tumor-to-muscle ratios of 873 ± 85 and 463 ± 90, respectively) and 72 hours p.i. (673 ± 350 and 359 ± 59, respectively). Although the contrast ratios were more modest in

GRANTA519 xenograft mice, there was still an increase from 14.2 ± 2.5 to 120 ± 45 tumor-to-blood ratio and 56.9 ± 20.0 to 90.6 ± 26.9 tumor-to-muscle ratio from 1 to 4 hours p.i. The corresponding SPECT images of [^{177}Lu]Lu-BL02 generally correlated well to the biodistribution data. Increased uptake was observed between 24 and 72 hours p.i. in SPECT images of Z138 xenografts. Autoradiography images of Z138 tumor sections showed heterogeneous uptake throughout the tumor, correlating with tumor tissue based on H&E staining (Supplementary Fig. S24).

Mouse and projected human dosimetry analysis of [^{177}Lu]Lu-BL02

On the basis of the Z138 and GRANTA519 longitudinal biodistribution, healthy organs in a 25 g standard mouse model receive low doses of ionizing radiation with the kidneys, the bone and the liver receiving the highest doses (Supplementary Fig. S25). The absorbed doses to the Z138 and GRANTA519 xenografts were 528 and 68.7 mGy/MBq, respectively. This led to high tumor-to-organ deposited dose ratios. Extrapolation to a healthy male human model showed relatively low amounts of ionizing radiation deposited into healthy tissues, with no organ receiving higher than 0.035 mGy per MBq injected. The kidneys (0.0332 and 0.0311 mGy/MBq, respectively) and liver (0.0183 and 0.0185 mGy/MBq)
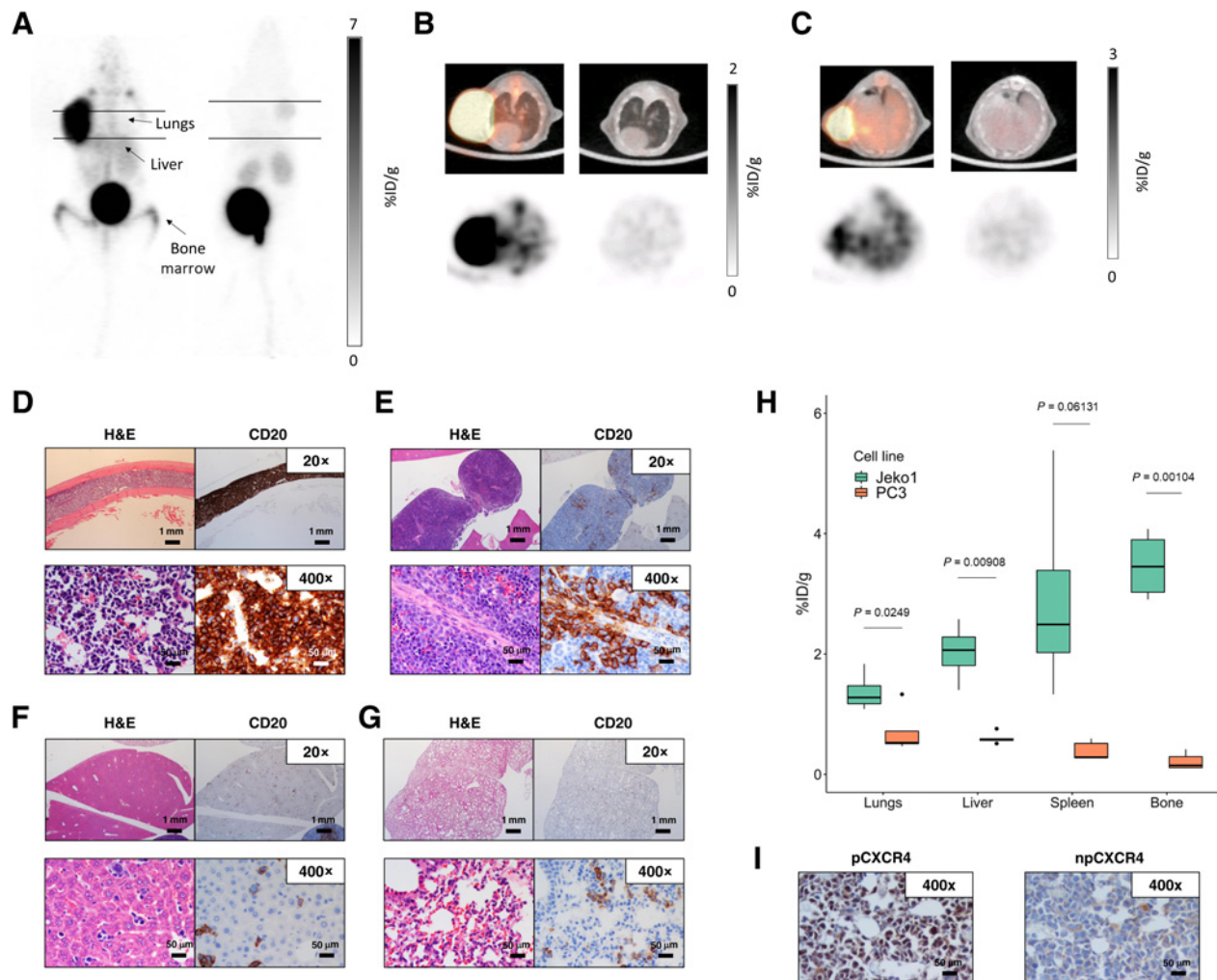
Figure 4.
A, Maximum intensity projections of PET images of [^{68}Ga]Ga-BL02 in Jeko1 metastatic model (left) and PC3 xenograft-bearing mice (right) at 1 hour p.i. The arrows point towards elevated areas of uptake corresponding to the rough anatomical location of indicated organs. The lines represent axial slices in **B** and **C**. Scale of the PET images is 0%ID/g to 7%ID/g. **B,** Axial PET images intersecting the lung of [^{68}Ga]Ga-BL02 in Jeko1 metastatic model (left) and PC3 xenograft-bearing mice (right) at 1 hour p.i. Scale of the PET images is 0%ID/g to 2%ID/g. **C,** Axial PET images intersecting the liver of [^{68}Ga]Ga-BL02 in Jeko1 metastatic model (left) and PC3 xenograft-bearing mice (right) at 1 hour p.i. Scale of the PET images is 0%ID/g to 3%ID/g. **D–G,** H&E and anti-CD20 IHC staining of (**D**) bone marrow, (**E**) spleen, (**F**) liver, and (**G**) lungs. **H,** Comparison of the *ex vivo* biodistribution of the lungs, liver, spleen, and bone in Jeko1 metastatic and PC3 xenograft models. **I,** Anti-npCXCR4 and anti-pCXCR4 IHC staining of the bone marrow of Jeko1 metastatic model.

were predicted to receive the highest radiation deposition per injected dose, respectively.

[^{177}Lu]Lu-BL02 rapidly induces MCL regression in xenograft mice

The high specificity of [^{177}Lu]Lu-BL02 led us to initiate radioligand therapy in Z138 xenograft mice. On the basis of the dosimetry of Z138 mice, we administered 28.2 ± 0.7 MBq, which corresponded to approximately 15 Gy deposited in the tumor and <25 mGy in healthy organs. Prior to treatment, no difference in tumor volumes were found between the treatment and control groups ($P = 0.152$). Longitudinal analysis of tumor volumes showed a clear treatment response, with a median time to remission of 9 days (**Fig. 5A**). In contrast, the control group showed positive exponential growth kinetics and had to be euthanized by 10 days due to humane endpoint criteria. Linear mixed

modeling of log-transformed data showed a clear difference in the growth trajectories between the two groups ($P < 0.0001$). The treatment group had a median survival of 27 days, whereas the control group had a median survival of 8 days ($P < 0.0001$), representing a greater than three-fold increase in survival (**Fig. 5B**). H&E staining of kidney tissues revealed no evidence of radiation-mediated acute tubular necrosis in treatment group (Supplementary Fig. S26).

[^{177}Lu]Lu-BL02-treated mice show concurrent metastasis during the regrowth phase

As the tumors grew back in the treatment group, 7 of 8 mice began to experience weight loss (**Fig. 5C**). One mouse was euthanized early due to weight loss and four others reached weight loss and tumor volume limits concurrently. We hypothesized that this was due to metastatic growth in peripheral tissues. H&E and anti-
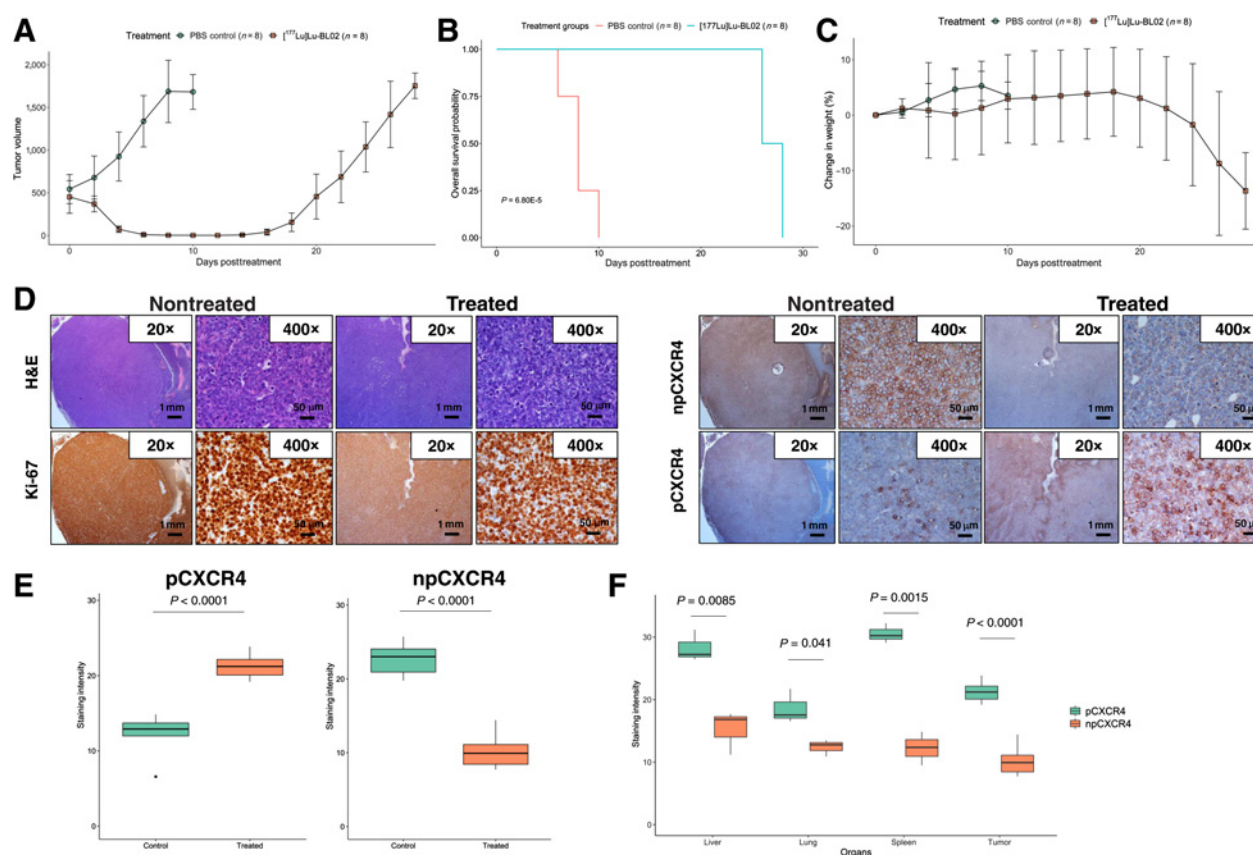
Figure 5.
A, Tumor growth curves of Z138 mantle cell lymphoma xenograft-bearing mice receiving either a single dose of [^{177}Lu]Lu-BL02 as treatment ($n = 8$) or phosphate-buffered saline as a control ($n = 8$; $P < 0.0001$). **B,** Kaplan–Meier curves depicting the length of survival of the [^{177}Lu]Lu-BL02 treatment group ($n = 8$) and saline control ($n = 8$; $P < 0.0001$). **C,** Percentage change in the weight of the mice in the [^{177}Lu]Lu-BL02 treatment group ($n = 8$) and the saline control group ($n = 8$) as a function of time until termination. **D,** Representative H&E, Ki-67, anti-npCXCR4, and anti-pCXCR4 staining of xenograft tissue collected from euthanized mice from the [^{177}Lu]Lu-BL02 treatment group ($n = 8$) and the saline control group ($n = 8$). **E,** Intensities of pCXCR4 and npCXCR4 IHC staining in the [^{177}Lu]Lu-BL02 treatment group ($n = 8$) and the saline control group ($n = 8$). **F,** Intensities of npCXCR4 and pCXCR4 IHC staining of the liver, lung, spleen, and Z138 xenografts of the mice in the [^{177}Lu]Lu-BL02 treatment group ($n = 8$).

CD20 IHC analysis showed significant infiltration of the tumor in the lungs, spleen, and liver (Supplementary Fig. S27). Comparison of the treated tumor to the control showed no difference in Ki-67 expression (96.1 ± 0.9% vs. 96.7 ± 1.0%, $P = 0.48$) and a significant increase in pCXCR4 expression over npCXCR4 ($P < 0.0001$; **Fig. 5D** and **E**). Metastatic cells in peripheral tissues showed a decrease in CD20 expression and a similar pCXCR4:npCXCR4 ratio (**Fig. 5F**).

Discussion

MCL has a heterogeneous clinical presentation and is associated with an overall poor prognosis, emphasizing the importance of risk stratification strategies and the development of additional lines of effective treatments. Herein we explored whether CXCR4 could be effectively targeted for PET imaging and radioligand therapy. To date, CXCR4 has been established as a biomarker for cancers with poor prognosis, shaping the tumor microenvironment, driving metastasis, and enhancing oncogenic signaling (15–17). Previous reports highlighted that CXCR4-mediating signaling enables migration of MCL cells to the bone marrow for chemoprotection, which may later manifest as resistant disease (14, 45). This was reflected in our

retrospective analysis of a single-center large MCL patient cohort, where positive CXCR4 expression was associated with poorer outcome, regardless of the receptor's functional state. CXCR4 expression was an independent marker of prognosis, even when adjusted for other prognostic variables. Finally, pCXCR4 expression, indicating a highly active CXCR4 signaling axis, was found throughout most of the cohort, highlighting the potential utility of CXCR4-directed imaging and therapy.

Previous studies reported the success of the UMB-2 antibody in accurately reporting surface-level CXCR4 expression (46, 47). Yet, due to the specificity of UMB-2 antibody towards an unphosphorylated sequence of the C-terminus of CXCR4, this antibody may be insensitive to phosphorylated variants, indicative of a microenvironment with a highly active CXCR4 signaling axis. This was confirmed with a proportionally low number of npCXCR4-POS patients in our cohort. Simultaneous assessment of phospho-Ser339 CXCR4 confirmed this lack of sensitivity. Using a pair of orthogonally sensitive anti-CXCR4 antibodies was essential in maximizing sensitivity for CXCR4 in our cohort.

In line with previous studies, our study shows that elevated expression of CXCR4 in patient MCL biopsies conferred a worse

prognosis (17). We further postulate that CXCR4 status is an important independent prognostic biomarker in MCL patient outcomes, although the pCXCR4-high$_{30}$ cut-off value requires further validation. CXCR4, therefore, represents a highly valuable target for molecular imaging and targeted therapy of MCL, especially by radioligand therapy.

Surprisingly, npCXCR4-POS MCLs had worse OS and PFS as compared with pCXCR4-high MCLs, a paradoxical result given that phosphorylation is indicative of activation of receptor signaling. It has been speculated that subpopulations of cells with unactivated CXCR4 are able to metastasize more easily by responding to extratumoral SDF-1 gradients (48), resulting in more disseminated and advanced disease. We showed correlation between npCXCR4-POS status to extranodal biopsy sites and worse ECOG and MIPI scores. A significant limitation of these interpretations, however, was the low number of npCXCR4-expressing patients. This may be due to the lack of antibody sensitivity, the proportionally lower number of extranodal sites sampled, or the relatively low occurrence of subpopulations of npCXCR4 within MCLs.

Preliminary investigations in the differential pathways that underlie pCXCR4-high and npCXCR4-POS cancers underscored a common theme of an immunologically cold tumor microenvironment. pCXCR4-high MCLs were characterized by upregulation of pathways that enabled cancer cell fitness that were absent in npCXCR4-POS MCLs, validating our approach with RNA-seq. Furthermore, we found downregulation of the T-cell receptor complex gene pathway in pCXCR4-high cancers, correlating with findings in breast and pancreatic cancers wherein CXCR4 signaling suppressed T-cell infiltration in cancers (49, 50). These results raise further questions as to the contribution of immune infiltrations, or lack thereof, to the disease course of MCLs and patient outcomes.

Having established the prognostic value of CXCR4 in MCLs, we aimed to leverage this for imaging and therapy. CXCR4-targeted molecular imaging by PET offers a complementary diagnostic approach alongside biopsies as a noninvasive modality capable of imaging the entire body and assessing receptor expression heterogeneity across metastatic sites. This approach can be further adapted as a radiotheranostic to deliver a therapeutic radioactive payload to sites of high target protein expression. Although antibody-based radiotheranostics have previously shown efficacy in hematologic malignancies, they suffer from nonspecific organ uptake and long circulation times, limiting their maximal administered dose (51, 52). In contrast, peptide-based radiotheranostics are a versatile alternative that have lower uptake in nontarget organs and are cleared quickly from circulation but still remain effective in target engagement given sufficient affinity (53).

Guided by *in silico* docking methods, we developed [^{68}Ga]Ga/[^{177}Lu]Lu-BL02 with improved contrast over an earlier compound (25). We established that [^{68}Ga]Ga- and [^{177}Lu]Lu-BL02 could specifically target CXCR4 protein expression, based on blocking controls and their application in xenograft models with varying expression levels of CXCR4. Both [^{68}Ga]Ga-BL02 and [^{177}Lu]Lu-BL02 also showed high and specific tumor uptake relative to nontarget tissues, essential for high-contrast lesion visualization and a high therapeutic index, respectively. Finally, autoradiography analysis showed heterogeneous but effective penetration of [^{177}Lu]Lu-BL02 throughout the xenograft.

Comparison with [^{68}Ga]Ga-Pentixafor, the current gold standard CXCR4 PET agent, further highlights the potential utility of [^{68}Ga]Ga-BL02 due to the latter's higher tumor uptake and lower nontarget organ accumulation. [^{68}Ga]Ga-BL02 could also delineate metastatic infiltration in Jeko1 xenograft mice. The low hepatobiliary and gastrointestinal uptake of [^{68}Ga]Ga-BL02 enabled detection of organs such as the liver infiltration by MCL. Combined, these results speak to the potential for sensitive and high-contrast PET imaging of various CXCR4-targeting malignancies.

For therapeutic studies in the Z138 model, we used a dose of 28 MBq, which corresponded to approximately 15 Gy based on dosimetry. This value is on the lower end of the range of doses expected to be effective in lymphomas (52) and, due to heterogeneous deposition, will not correlate perfectly with external beam dosimetry. Although dosimetry analysis of [^{177}Lu]Lu-BL02 indicated a low burden of radioactivity in healthy tissues, these results may not be completely predictive of human studies as LY2510924 has an approximately 35-fold poorer affinity for mouse CXCR4 over human CXCR4 (54). However, in comparison to [^{177}Lu]Lu-DOTA-r-a-ABA-CPCR4, an improved Pentixather derivative, [^{177}Lu]Lu-BL02 showed faster clearance and lower nontarget organ uptake based on published literature values (55). Combined with the higher uptake shown by [^{68}Ga]Ga-BL02 over [^{68}Ga]Ga-Pentixafor, we expect [^{177}Lu]Lu-BL02 to have high accumulation of radioactivity in CXCR4-expressing cancers with comparatively lower off-target radiotoxicity, enhancing its therapeutic index. Given the known expression of CXCR4 in hematopoietic stem cells (56) and T lymphocytes (57), marrow toxicity is anticipated from CXCR4-targeted radioligand therapy and human studies will be required to evaluate potential toxicity.

Although [^{177}Lu]Lu-BL02-treated mice responded effectively toward treatment, metastatic growth accompanied the regrowth of the MCL xenograft. Further investigation revealed an enhanced pCXCR4:npCXCR4 ratio in the regrown xenograft and metastatic organs. This mirrored the correlation of recurrent disease with pCXCR4-high MCL patients and the enhanced pCXCR4:npCXCR4 ratio in the marrow of the Jeko1 metastatic model. Enhanced CXCR4/SDF-1 signaling has been reported post-radiation therapy; the induction of hypoxia in the locally treated tissues lead an upregulation of CXCR4 signaling, resulting in the recruitment of stromal and immune cells for vasculogenesis and tumor regrowth (58). Increase in pCXCR4:npCXCR4 ratio was also observed in higher grade astrocytomas, further implicating CXCR4 as one of the culprits in this enhanced aggressive phenotype (59). Finally, our differential analysis showed that pCXCR4-high tumors had elevated expression of genes implicated in DNA repair, implicating pCXCR4 signaling as a potential protective mechanism. Therefore, activation of CXCR4 may represent an important determinant in patient response post-radioligand therapy. Furthermore, it appears that total CXCR4 expression was relatively unchanged between the treated and control groups. As such, higher administered activities or additional doses of [^{177}Lu]Lu-BL02 may be considered to enhance the effectiveness and duration of response, given the low dose delivered to nontarget organs. Additional preclinical and future clinical studies are ongoing to assess the efficacy of this approach.

Conclusion

We established that pCXCR4 and npCXCR4 are independent prognostic factors for outcomes in patients with MCL and a promising target for intervention. We characterized [^{68}Ga]Ga/[^{177}Lu]Lu-BL02, a CXCR4-targeting radiotheranostic pair, in a preclinical study to assess its potential to detect, stage, and treat MCL patients. CXCR4-targeted radioligand therapy is a promising approach to treat MCL and warrants further clinical translation.

Authors' Disclosures

Authors' Contributions

D. Kwon: Conceptualization, resources, data curation, software, formal analysis, validation, investigation, visualization, methodology, writing–original draft, project administration, writing–review and editing. **K. Takata:** Conceptualization, resources, data curation, formal analysis, investigation, visualization, methodology, project administration, writing–review and editing. **Z. Zhang:** Resources, data curation, investigation, visualization, methodology. **L. Chong:** Resources, data curation, software, validation, visualization, project administration, writing–review and editing. **B. Fraser:** Data curation, software, formal analysis, visualization, methodology. **J. Zeisler:** Formal analysis, validation, visualization. **T. Miyata-Takata:** Formal analysis, validation, investigation. **H. Merkens:** Resources, data curation, visualization, methodology. **J. Rousseau:** Resources, data curation, visualization. **T. Aoki:** Resources, visualization, methodology. **H.-T. Kuo:** Resources, methodology. **R. Tan:** Resources, methodology. **C. Zhang:** Resources. **J. Lau:** Conceptualization, writing–review and editing. **D. Villa:** Resources. **C.F. Uribe:** Resources, investigation, visualization, methodology, writing–review and editing. **K.-S. Lin:** Conceptualization, project administration, writing–review and editing. **C. Steidl:** Conceptualization, resources, supervision, funding acquisition, project administration, writing–review and editing. **F. Benard:** Conceptualization, resources, supervision, funding acquisition, project administration, writing–review and editing.

Acknowledgments

References

1. Maddocks K. Update on mantle cell lymphoma. Blood 2018;132:1647–56.
2. Vose JM. Mantle cell lymphoma: 2017 update on diagnosis, risk-stratification, and clinical management. Am J Hematol 2017;92:806–13.
3. Hoster E, Dreyling M, Klapper W, Gisselbrecht C, Van Hoof A, Kluin-Nelemans HC, et al. A new prognostic index (MIPI) for patients with advanced-stage mantle cell lymphoma. Blood 2008;111:558–65.
4. Aukema SM, Hoster E, Rosenwald A, Canoni D, Delfau-Larue MH, Rymkiewicz G, et al. Expression of TP53 is associated with the outcome of MCL independent of MIPI and Ki-67 in trials of the European MCL Network. Blood 2018;131:417–20.
5. Ladha A, Zhao J, Epner EM, Pu JJ. Mantle cell lymphoma and its management: where are we now? Exp Hematol Oncol 2019;8:2.
6. Lenz G, Dreyling M, Hoster E, Wörmann B, Dührsen U, Metzner B, et al. Immunochemotherapy with rituximab and cyclophosphamide, doxorubicin, vincristine, and prednisone significantiy improves response and time to treatment failure, but not long-term outcome in patients with previously untreated mantle cell lymphoma: results of a prospective randomized trial of the German Low Grade Lymphoma Study Group (GLSG). J Clin Oncol 2005;23:1984–92.
7. Hermine O, Hoster E, Walewski J, Ribrag V, Brousse N, Thieblemont C, et al. Alternating courses of 3x CHOP and 3x DHAP plus rituximab followed by a high dose ARA-C containing myeloablative regimen and autologous stem cell transplantation (ASCT) increases overall survival when compared to 6 courses of CHOP plus rituximab followed by myeloablative radiochemotherapy and ASCT in mantle cell lymphoma: final analysis of the MCL Younger Trial of the European Mantle Cell Lymphoma Network (MCL net). Blood 2012;120:151.
8. Maddocks K, Christian B, Jaglowski S, Flynn J, Jones JA, Porcu P, et al. A phase 1/1b study of rituximab, bendamustine, and ibrutinib in patients with untreated and relapsed/refractory non-Hodgkin lymphoma. Blood 2015;125:242–8.
9. Ruan J, Martin P, Furman RR, Lee SM, Cheung K, Vose JM, et al. Bortezomib plus CHOP-rituximab for previously untreated diffuse large B-cell lymphoma and mantle cell lymphoma. J Clin Oncol 2011;29:690–7.
10. Pu JJ, Ehmann WC, Liao J, Capper C, Levy M, Claxton DF, et al. The results of a phase I study using velcade (Bortezomib), cladribine, and rituximab (VCR) in treating mantle cell lymphoma. Blood 2016;128:1792.
11. Wang M, Fayad L, Wagner-Bartak N, Zhang L, Hagemeister F, Neelapu SS, et al. Lenalidomide in combination with rituximab for patients with relapsed or refractory mantle-cell lymphoma: a phase 1/2 clinical trial. Lancet Oncol 2012;13:716–23.
12. Liu H, Johnson JL, Koval G, Malnassy G, Sher D, Damon LE, et al. Detection of minimal residual disease following Induction Immunochemotherapy predicts progression free survival in mantle cell lymphoma: final results of CALGB 59909. Haematologica 2012;97:579–85.
13. Pott C, Macintyre E, Delfau-Larue M-H, Ribrag V, Unterhalt M, Kneba M, et al. MRD eradication should be the therapeutic goal in mantle cell lymphoma and may enable tailored treatment approaches: results of the Intergroup Trials of the European MCL Network. Blood 2014;124:147.
14. Kurtova AV, Tamayo AT, Ford RJ, Burger JA. Mantle cell lymphoma cells express high levels of CXCR4, CXCR5, and VLA-4 (CD49d): importance for interactions with the stromal microenvironment and specific targeting. Blood 2009;113:4604–13.

15. Guo F, Wang Y, Liu J, Mok SC, Xue F, Zhang W. CXCL12/CXCR4: a symbiotic bridge linking cancer cells and their stromal neighbors in oncogenic communication networks. Oncogene 2016;35:816–26.

16. Chatterjee S, Behnam Azad B, Nimmagadda S. The intricate role of CXCR4 in cancer. Advances in Cancer Research. 1st ed. Elsevier Inc.; 2014. p. 31–82.

17. Zhao H, Guo L, Zhao H, Zhao J, Weng H, Zhao B. CXCR4 over-expression and survival in cancer: a system review and meta-analysis. Oncotarget 2015;6: 5022–40.

18. Jadvar H, Chen X, Cai W, Mahmood U. Radiotheranostics in cancer diagnosis and management. Radiology 2018;286:388–400.

19. Herrmann K, Schwaiger M, Lewis JS, Solomon SB, McNeil BJ, Baumann M, et al. Radiotheranostics: a roadmap for future development. Lancet Oncol 2020;21: e146–56.

20. Sgouros G, Kolbert KS, Sheikh A, Pentlow KS, Mun EF, Barth A, et al. Patient-specific dosimetry for 131I thyroid cancer therapy using 124I PET and 3-Dimensional-Internal Dosimetry (3D-ID) software. J Nucl Med 2004; 45:1366–72.

21. Hennrich U, Kopka K. Lutathera®: the first FDA-and EMA-approved radiopharmaceutical for peptide receptor radionuclide therapy. Pharmaceuticals 2019;12:114.

22. Hofman MS, Violet J, Hicks RJ, Ferdinandus J, Ping Thang S, Akhurst T, et al. [177Lu]-PSMA-617 radionuclide treatment in patients with metastatic castration-resistant prostate cancer (LuPSMA trial): a single-centre, single-arm, phase 2 study. Lancet Oncol 2018;19:825–33.

23. Lapa C, Schreder M, Schirbel A, Samnick S, Kortüm KM, Herrmann K, et al. [68Ga]Pentixafor-PET/CT for imaging of chemokine receptor CXCR4 expression in multiple myeloma - Comparison to [18 F]FDG and laboratory values. Theranostics 2017;7:205–12.

24. Herrmann K, Schottelius M, Lapa C, Osl T, Poschenrieder A, Hänscheid H, et al. First-in-human experience of CXCR4-directed endoradiotherapy with 177Lu- and 90Y-labeled pentixather in advanced-stage multiple myeloma with extensive intra- and extramedullary disease. J Nucl Med 2016;57:248–51.

25. Lau J, Kwon D, Rousseau E, Zhang Z, Zeisler J, Uribe CF, et al. Ga/[177Lu]Lu-BL01, a novel theranostic pair for targeting C-X-C chemokine receptor 4. Mol Pharm 2019;16:4688–95.

26. Pararajalingam P, Coyle KM, Arthur S, Thomas N, Alcaide M, Meissner B, et al. Coding and non-coding drivers of mantle cell lymphoma identified through exome and genome sequencing. Blood 2020;136:572–84.

27. Moreno MJ, Bosch R, Dieguez-Gonzalez R, Novelli S, Mozos A, Gallardo A, et al. CXCR4 expression enhances diffuse large B cell lymphoma dissemination and decreases patient survival. J Pathol 2015;235:445–55.

28. Love MI, Huber W, Anders S. Moderated estimation of fold change and dispersion for RNA-seq data with DESeq2. Genome Biol 2014;15:550.

29. Huang DW, Sherman BT, Lempicki RA. Systematic and integrative analysis of large gene lists using DAVID bioinformatics resources. Nat Protoc 2009;4: 44–57.

30. Huang DW, Sherman BT, Lempicki RA. Bioinformatics enrichment tools: paths toward the comprehensive functional analysis of large gene lists. Nucleic Acids Res 2009;37:1–13.

31. Ashburner M, Ball CA, Blake JA, Botstein D, Butler H, Cherry JM, et al. Gene Ontology: tool for the unification of biology. Nat Genet 2000;25:25–9.

32. Carbon S, Douglass E, Good BM, Unni DR, Harris NL, Mungall CJ, et al. The Gene Ontology resource: enriching a GOld mine. Nucleic Acids Res 2021;49: D325–34.

33. Ogata H, Goto S, Sato K, Fujibuchi W, Bono H, Kanehisa M. KEGG: Kyoto Encyclopedia of Genes and Genomes. Nucleic Acids Res 1999;27:29–34.

34. Rouillard AD, Gundersen GW, Fernandez NF, Wang Z, Monteiro CD, McDermott MG, et al. The harmonizome: a collection of processed datasets gathered to serve and mine knowledge about genes and proteins. Database 2016;2016:baw100.

35. Subramanian A, Tamayo P, Mootha VK, Mukherjee S, Ebert BL, Gillette MA, et al. Gene set enrichment analysis: a knowledge-based approach for interpreting genome-wide expression profiles. Proc Natl Acad Sci U S A 2005;102: 15545–50.

36. Mootha VK, Lindgren CM, Eriksson K-F, Subramanian A, Sihag S, Lehar J, et al. PGC-1α-responsive genes involved in oxidative phosphorylation are coordinately downregulated in human diabetes. Nat Genet 2003;34:267–73.

37. Barretina J, Caponigro G, Stransky N, Venkatesan K, Margolin AA, Kim S, et al. The Cancer Cell Line Encyclopedia enables predictive modelling of anticancer drug sensitivity. Nature 2012;483:603–7.

38. Fischer T, Nagel F, Jacobs S, Stumm R, Schulz S. Reassessment of CXCR4 chemokine receptor expression in human normal and neoplastic tissues using the novel rabbit monoclonal antibody UMB-2. PLoS One 2008;3:e4069.

39. Mueller W, Schütz D, Nagel F, Schulz S, Stumm R. Hierarchical organization of multi-site phosphorylation at the CXCR4 C terminus. PLoS One 2013;8:e64975.

40. Peng S, Zhang X, Paul D, Kays LM, Gough W, Stewart J, et al. Identification of LY2510924, a novel cyclic peptide CXCR4 antagonist that exhibits antitumor activities in solid tumor and breast cancer metastatic models. Mol Cancer Ther 2015;14:480–91.

41. Poschenrieder A, Schottelius M, Schwaiger M, Kessler H, Wester H-J. The influence of different metal-chelate conjugates of pentixafor on the CXCR4 affinity. EJNMMI Res 2016;6:36.

42. Wu B, Chien EYT, Mol CD, Fenalti G, Liu W, Katritch V, et al. Structures of the CXCR4 chemokine GPCR with small-molecule and cyclic peptide antagonists. Science 2010;330:1066–71.

43. Stephens BS, Ngo T, Kufareva I, Handel TM. Functional anatomy of the full-length CXCR4-CXCL12 complex systematically dissected by quantitative model-guided mutagenesis. Sci Signal 2020;13:eaay5024.

44. Jeon HJ, Kim CW, Yoshino T, Akagi T. Establishment and characterization of a mantle cell lymphoma cell line. Br J Haematol 1998;102:1323–6.

45. Chen Z, Teo AE, McCarty N. ROS-induced CXCR4 signaling regulates mantle cell lymphoma (MCL) cell survival and drug resistance in the bone marrow microenvironment via autophagy. Clin Cancer Res 2016;22:187–99.

46. Weiss ID, Huff LM, Evbuomwan MO, Xu X, Dang HD, Velez DS, et al. Screening of cancer tissue arrays identifies CXCR4 on adrenocortical carcinoma: correlates with expression and quantification on metastases using 64Cu-plerixafor PET. Oncotarget 2017;8:73387–406.

47. Wyler L, Napoli CU, Ingold B, Sulser T, Heikenwälder M, Schraml P, et al. Brain metastasis in renal cancer patients: metastatic pattern, tumour-associated macrophages and chemokine/chemoreceptor expression. Br J Cancer 2014; 110:686–94.

48. Balkwill F. Cancer and the chemokine network. Nat Rev Cancer 2004;4:540–50.

49. Chen IX, Chauhan VP, Posada J, Ng MR, Wu MW, Adstamongkonkul P, et al. Blocking CXCR4 alleviates desmoplasia, increases T-lymphocyte infiltration, and improves immunotherapy in metastatic breast cancer. Proc Natl Acad Sci U S A 2019;116:4558–66.

50. Feig C, Jones JO, Kraman M, Wells RJB, Deonarine A, Chan DS, et al. Targeting CXCL12 from FAP-expressing carcinoma-associated fibroblasts synergizes with anti-PD-L1 immunotherapy in pancreatic cancer. Proc Natl Acad Sci U S A 2013; 110:20212–7.

51. Forrer F, Oechslin-Oberholzer C, Campana B, Herrmann R, Maecke HR, Mueller-Brand J, et al. Radioimmunotherapy with 177Lu-DOTA-rituximab: final results of a phase I/II study in 31 patients with relapsing follicular, mantle cell, and other indolent B-cell lymphomas. J Nucl Med 2013;54:1045–52.

52. Larson SM, Carrasquillo JA, Cheung NKV, Press OW. Radioimmunotherapy of human tumours. Nat Rev Cancer 2015;15:347–60.

53. Blok D, Feitsma RIJ, Vermeij P, Pauwels EJK. Peptide radiopharmaceuticals in nuclear medicine. Eur J Nucl Med 1999;26:1511–9.

54. Peng SB, Van Horn RD, Yin T, Brown RM, Roell WC, Obungu VH, et al. Distinct mobilization of leukocytes and hematopoietic stem cells by CXCR4 peptide antagonist LY2510924 and monoclonal antibody LY2624587. Oncotarget 2017; 8:94619–34.

55. Osl T, Schmidt A, Schwaiger M, Schottelius M, Wester H-J. A new class of PentixaFor- and PentixaTher-based theranostic agents with enhanced CXCR4-targeting efficiency. Theranostics 2020;10:8264–80.

56. Burger JA, Kipps TJ. CXCR4: a key receptor in the crosstalk between tumor cells and their microenvironment. Blood 2006;107:1761–7.

57. Bleul CC, Wu L, Hoxie JA, Springer TA, Mackay CR. The HIV coreceptors CXCR4 and CCR5 are differentially expressed and regulated on human T lymphocytes. Proc Natl Acad Sci U S A 1997;94:1925–30.

58. Tseng D, Vasquez-Medrano DA, Brown JM. Targeting SDF-1/CXCR4 to inhibit tumour vasculature for treatment of glioblastomas. Br J Cancer 2011;104:1805–9.

59. Woerner BM, Warrington NM, Kung AL, Perry A, Rubin JB. Widespread CXCR4 activation in astrocytomas revealed by phospho-CXCR4-specific antibodies. Cancer Res 2005;65:11392–9.